Adsorption performance and optimization by response surface methodology on tetracycline using Fe-doped ZIF-8 loaded with multi-walled carbon nanotubes

Jiacheng Li
Nanjing Forestry University

Tian Tian
Nanjing Forestry University

Yannan Jia
State Key Laboratory of Simulation and Regulation of Water Cycle in River Basin

Nannan Xu
State Key Laboratory of Simulation and Regulation of Water Cycle in River Basin

Shujun Yang
State Key Laboratory of Simulation and Regulation of Water Cycle in River Basin

Chenyue Zhang
Nanjing Forestry University

Shiwei Gao
Nanjing Forestry University

Wei Shen
Nanjing Municipal Design and Research Institute Co., Ltd.

zheng wang (✉ wangzheng@njfu.edu.cn)
Nanjing Forestry University   https://orcid.org/0000-0003-4882-380X

Research Article

Abstract

A metal-organic framework material, an iron-doped ZIF-8 loaded with multi-walled carbon nanotubes (FZM), was fabricated and used to adsorb tetracycline (TC) in this investigation. The adsorption impact and mechanism of TC on FZM were revealed using batch adsorption experiments and characterization analyses. The effects of Fe doping amount, pH, temperature, beginning concentration, and coexisting ions on the adsorption effect of TC were explored. It was discovered that Fe doping amount of 75 mg, pH of 6, and initial concentration of 100 mg/L produced the optimum adsorption effect. TC adsorption was also enhanced by the presence of Ca^{2+}. The adsorption process of TC on FZM followed the pseudo-second-order (PSO) kinetic and Freundlich isotherm models, indicating that chemisorption was the dominant factor in the removal process of TC and the reaction was multilayer adsorption, with a theoretical maximum saturation capacity of 1111.11 mg/g fitted according to the Langmuir model, which was better than most other adsorbents. The procedure of TC adsorption on FZM. The adsorption process on FZM is a spontaneous, heat-absorbing process, and the adsorption capacity increases as the temperature rises. According to the findings of the FTIR study undertaken before and after adsorption, the mechanism of TC on FZM is predominantly intermolecular hydrogen bonding, surface complexation, π-π interactions, and electrostatic interactions. The projected adsorption capacity of TC was 599.78 mg/g under optimal adsorption circumstances of pH 7.1, temperature 312.5 K, and injection amount 64.43 mg/L, with a divergence of 1.73 % from the actual value, according to the response surface optimization studies. Furthermore, FZM has high reusability, and after four cycles of trials, the adsorption capacity of TC on FZM may still be greater than 370 mg/g, with a 15% loss. The cost of treating 100 mg/L of TC effluent was estimated to be around 8.35 US\$/m^3, indicating that FZM had excellent application possibilities for TC removal.

1. Introduction

In recent decades, antibiotics have been identified in significant amounts in water bodies and terrestrial ecosystems(Liu et al. 2018). TC has become one of the most widely prescribed in the world, with its efficient antimicrobial property in underdeveloped nations, and is extensively utilized in the treatment of various ailments and livestock breeding(Akbari et al. 2021). TC, on the other hand, is not thoroughly absorbed by the body, and 70-90% of it is excreted in the sewage system via urine and feces(Minale et al. 2020). TC will migrate into the surroundings through domestic sewage and industrial effluents if it is not completely eliminated, contaminating the ecological system and posing a risk to public health and aquatic ecology(Zhou et al. 2021). Furthermore, TC is biodegradable, whereas enormous concentrations of TC suppress the activity of microorganisms(Wang et al. 2021). TC has low toxicity, but it produces adverse effects in humans such as nausea and vomiting, as well as an inhibitory effect on microorganisms in the environment(Chen et al. 2020). Antibiotic resistance genes triggered by antibiotic misuse are predicted to cause 10 million deaths by the middle of this century. Hence, the elimination of TC is a pressing environmental issue that must be addressed immediately.

Proper treatment before discharge is required to reduce TC release into the environment(Ashworth & Ibekwe 2020). Photodegradation(Norvill et al. 2017), biodegradation(Huang et al. 2014), electrochemical degradation(Brinzila et al. 2012), sonochemical degradation(Nasseri et al. 2017) and adsorption(Minale et al. 2020) have all been employed to remove TC from aquatic environments for decades. TC has been removed from water using these methods. Nevertheless, adsorption is an extensively employed methodology for eliminating TC from aqueous solution cost-effectively and efficiently. TC was collected by using variety of adsorbents, including biochar(Liu et al. 2021; Li et al. 2021), kaolinite(Zhao et al. 2011), chitosan(Yaqubi et al. 2021), ceramsite(Zhang et al. 2019), carbohydrate-based carbon(Wang et al. 2021) and reduced graphene oxide(Bao et al. 2018). Because these materials have a limited adsorption ability, the demand for high-efficiency adsorbents for contaminant removal is still increasing.

Metal-organic frameworks (MOFs) are one-of-a-kind composites with properties including porosity, high surface area, and structural flexibility(Feng et al. 2019; Vo and Kim 2021). The nanomaterials derived from the reaction of metal ions as the center and imidazole as an organic ligand, zeolitic imidazolate frameworks (ZIFs), one of the high thermal and water durability among these MOFs(Fei et al. 2013). Especially in recent decades, ZIFs have been shown to function well in gas separation(Wang et al. 2015), photocatalysis(Huang et al. 2021), and desalination(Wei et al. 2020), particularly in terms of adsorption(Li et al. 2020). For example, Ding et al. employed ZIF-8 to capture Cr(VI), methyl orange(MO), and phenol, exhibiting encouraging results(Ding et al. 2017). In addition, ZIFs have been explored for their potential to be integrated with various materials via post-synthesis processes to enhance their adsorption effectiveness. Wang et al. effectively generated ZIF-8/hydroxylated MWCNT nanocomposites, and the adsorption capacity of phosphate reaches 203 mg/g(Wang et al. 2020). Pei et al. applied phosphorylated iron-doped ZIF-8 to adsorb U(VI) and discovered that the adsorption capacity reached 631 mg/g(Pei et al. 2022). Within those trials, it was established that the ZIF-8 has greater performance in eliminating unwanted contaminants. However, the Fe-doped ZIF-8/ MWCNTs composite has yet to be investigated as a TC adsorbent in an aqueous solution.

In this paper, iron-doped ZIF-8/MWCNTs for TC removal from wastewater was prepared using a post-synthesis approach. The influences of pH value, reaction time, and primary TC concentration were all systematically discussed to evaluate the adsorption behavior of FZM for TC. The adsorption kinetics, isotherms, and thermodynamics of TC on FZM were also explored in-depth to further explain the mechanisms. Response surface methodology (RSM) and Box-Behnken design (BBD) were utilized to simulate FZM's removal effect on TC. The optimum conditions were identified by adjusting three parameters: pH, adsorbent dosage, and temperature, all of which were tested. Finally, the FZM material's production cost was estimated, and repeated regeneration trials were conducted to investigate the feasibility of its practical application.

2. Materials And Methods

2.1. Reagents

Zinc nitrate hexahydrate ($Zn(NO_3)_2 \cdot 6H_2O$, ≥99%) was purchased from Chemical Reagent Co., Ltd. (Nanjing, China), 2-methylimidazole ($C_4H_6N_2$, 99%) was purchased from Aladdin Biochemical Technology Co., Ltd. (Shanghai, China), heptahydrate Ferrous sulfate ($FeSO_4 \cdot 7H_2O$, ≥99%), methanol (CH_4O, ≥99.5%) were purchased from Sinopharm Chemical Reagent Co., Ltd. Tetracycline (99%) and multi-walled carbon nanotubes (>95%, outer diameter: 8-15 nm, length: ~50 μm) were provided by McLean Biochemical Technology Co., Ltd (Shanghai, China). Without additional treatment, all reagents were utilized as purchased.

2.2 Synthesis of adsorbents

2.2.1 Preparation of ZIF-8 and Fe-ZIF-8

The preparations for ZIF-8 and Fe-ZIF-8 adopt the simple precipitation method. To be more specific, 1.5g of $Zn(NO_3)_2 \cdot 6H_2O$ and 75mg of $FeSO_4 \cdot 7H_2O$ were dissolved in 70mL of methanol (solution A), and 3.3g of 2-methylimidazole was dissolved in 70mL of methanol (solution B). After stirring for 30 minutes and generating a homogeneous solution, solution B was gently added to solution A to make a mixed solution. The mixture was then stirred vigorously for 3 hours at room temperature. After that, the combination was allowed to rest for 1 day in an indoor environment. Finally, the solid was rinsed three times using anhydrous methanol after centrifuging the emulsion at 8000 rpm. The solid was dried in a vacuum at 60 °C for 12 hours to obtain a white ZIF-8 powder and a light-yellow Fe-ZIF-8 powder. Moreover, Fe-ZIF-8 (0) and Fe-ZIF-8 (150) were prepared similarly to Fe-ZIF-8 (75), with the addition of $FeSO_4 \cdot 7H_2O$ was 0 mg and 150 mg, respectively.

2.2.2 Preparation of Fe doped ZIF-8/MWCNTs composite

Fe-ZIF-8/MWCNTs was synthesized by a post-synthesis method. Following that, 10mg of multi-walled carbon nanotubes were added to the previously prepared Fe-ZIF-8 solution, which was then ultrasonically stirred for 30 minutes and magnetically stirred for 3 hours to form a uniformly dispersed mixture. The mixture is then deposited in a polytetrafluoroethylene-lined autoclave and maintained at 90 °C for 12 hours. Collect the sample after the reaction is finished, rinse it 3 times using methanol and ultrapure water, and then place it in a vacuum at 60 °C for 12 h to acquire the final product.

2.3 Sample analysis

The crystal structures of the samples were obtained by X-ray diffraction (XRD; Ultima IV, Rigaku, Japan). The power of the Cu-kα X-ray generator was 3 kW, the scanning speed was 0.02 °/s, and the 2θ test range was 5°−50°.

To observe the morphologies of the materials, high-resolution images of gold-plated samples were taken using scanning electron microscopy (SEM; JSM-7600f, Jeol, Japan; accelerating voltage 20 kV).

The chemical compositions of the samples were analyzed by Fourier-transform infrared (FT-IR) spectroscopy (Nicolet IS5, Thermo Scientific, USA) in the wavenumber range 400–4000 cm^{-1}.

The Brunauer-Emmett-Teller (BET) specific surface areas, pore-size distributions, and pore volumes of samples were determined using an automatic specific surface area and pore size analyzer (ASAP2020 and HD88, Micromeritics, USA).

N_2 adsorption-desorption isotherms were obtained at −196 °C after degassing at 150 °C for 24 h (heating rate 10 °C/min, N_2 flow rate 30 mL/min, test range room temperature to 800 °C).

The thermal stabilities of the samples were evaluated by thermogravimetric analysis (TGA; Q500, Ta, USA)

X-ray photoelectron spectroscopy (XPS; ESCALAB 250Xi, Thermo Scientific, USA) was used to obtain species, valence, and composition information for the sample surface elements.

2.4 Evaluation of adsorption performance

In batch experiments, the adsorption properties of as-prepared adsorbents for TC were studied. All of the TC solutions were made from the 100-mg/L stock solution, which was developed by dissolving quantitative TC powder in ultrapure water and preserving it at 4°C in the refrigerator.

A centrifuge tube containing 50 mL of TC solution (100 mg/L) was infused with a specified amount of adsorbent and placed in a constant temperature oscillator at 160 rpm and 298 K to evaluate the effect of adsorbent dosage, solution pH, and co-existing ionic strength. The solution pH was adjusted from 2 to 12 using 0.1mol/L HCl and 0.1mol/L NaOH. The effect of ionic strength on TC adsorption by FZM at various concentrations (50, 100mg/L) was researched using NaCl, Na_2SO_4, Na_2CO_3, $MgCl_2$, and $CaCl_2$. After adsorption, a 0.22-μm filter was used to obtain a clear solution, and the residual TC concentration was detected using an ultraviolet spectrophotometer at 357nm, and the removal rate (R) and adsorption capacity (Q_e, mg/g) were estimated by equations 2.1 and 2.2.

$$R = \frac{C_i - C_e}{C_i} \times 100\% \qquad (2.1)$$

$$Q_e = \frac{(C_i - C_e)V}{m} \times 100\% \qquad (2.2)$$

In which, C_i and C_e are the concentration of TC before and after reaction, respectively, mg/L; V is the volume of TC solution, mL; m is the amount of adsorbents, mg.

2.5 Optimization by RSM

RSM is a statistical approach for fitting correlations between factors and response values that employs quadratic polynomial equations. It requires consideration of experimental features such as experiment design, model applicability, and the ideal combination of conditions. The BBD model of RSM was used to explore the effect of three significant individual variables on TC adsorption capacity on FZM, including pH (A, 4-8), temperature (B, 298−318 K), and adsorbent dosage (C, 50-150 mg/L), as well as the projected response (Y) to the adsorption capacity. The TC optimization criteria are described in Table S1.

Use Design-Expert 12 software for statistical investigations such as analysis of variance (ANOVA), 3D surface plots, and fit statistics. A binary regression equation is used to represent the relationship between the response variable (Y) and the individual variable (X), as shown below (Equation 2.3).

$$Y=\beta_0+\sum_{i=1}^{K}\beta_i X_i + \sum_{i=1}^{K}\beta_{ii}X_i^2 + \sum_{i}^{K-1}\sum_{j}^{K}\beta_{ij}X_iX_j \qquad (2.3)$$

Where Y is the predicted response; X_i and X_j are the independent variables (*i* and *j* = 1, 2, 3, 4, or k); and β_0, β_i, β_{ii}, and β_{ij} are the migration, linear, second-order, and interaction coefficients, respectively.

3. Results And Discussion

3.1 Characterization

3.1.1 SEM analysis

SEM images of ZIF-8, MWCNTs, Fe-ZIF-8, and FZM are shown in Fig. 1. The microstructure and morphology of the ZIF-8 crystal demonstrate that it is rhombohedral in shape, which is in accordance with previous observations. However, once compared to the original ZIF-8, the crystal structure of ZIF-8 after Fe doping exhibits an obvious collapse, which could be consistent with the notion that only a small portion of Fe^{2+} is introduced into the ZIF-8 framework to replace Zn^{2+}, and the remainder was oxidized to Fe^{3+} and dispersed on the surface and pores of Fe-ZIF-8, causing the framework's stability to be compromised and the structure to collapse(Pei et al. 2022). FZM has a chain structure. Fe-ZIF-8 adheres to and grows around MWCNTs, and MWCNTs intersperse inside the Fe-ZIF-8 crystal, joining adjacent

crystal particles in series, as seen in Fig. 1(d). It's possible that Zn^{2+} gets adsorbed on MWCNTs' surfaces, resulting in the Fe-ZIF-8 production process taking place there(Zhang et al. 2021).

3.1.2 XRD analysis

Figure 2(a) shows the X-ray diffraction patterns of ZIF-8, MWCNTs, Fe-ZIF-8, and FZM. It can be seen that there are obvious characteristic peaks similar to ZIF-8 in the XRD pattern of FZM composites, which are located at 7.5°, 10.5°, 12.5°, 14.7°, 16.2°, and 18.0° corresponding to the characteristic diffraction peaks of (011), (002), (112), (022), (013) and (222) crystal planes(Wang et al. 2020). Compared with the XRD patterns of ZIF-8 and Fe-ZIF-8, FZM showed stronger peak intensity around 2θ = 26°, indicating that ZIF-8 and MWCNTs were successfully recombined. In addition, the high-intensity characteristic peaks indicate that the synthesized sample has high crystallinity, and at the same time, no other obvious peaks are observed, indicating that the sample is well synthesized.

3.1.3 FTIR analysis

FTIR spectra were utilized to characterize the samples and analyze the functional groups contained in them. Figure 2(b) depicts the FTIR profiles of four samples: MWCNTs, ZIF-8, Fe-ZIF-8, and FZM. The profiles of ZIF-8 and Fe-ZIF-8 are nearly identical, implying that the Fe doping modification did not affect the functional group species of ZIF-8. From the figure, the absence of broad peaks in the wavenumber between 3300 and 3500 cm^{-1} is due to the successful binding of N-H to Zn(Tsai et al. 2019). The absorption of the telescopic vibrations of C-H belonging to the saturated hydrocarbon C-H (CH_3) and the unsaturated hydrocarbon C-H of 2-methylimidazole, respectively, causes the characteristic peaks at 2931 and 3135 cm^{-1}. The telescopic vibrations of Zn-N are responsible for the sharp peak at 423 cm^{-1}, indicating that Zn is attached to the nitrogen atom to form a ligand structure(Nagarjun & Dhakshinamoorthy 2019). Furthermore, the characteristic peaks in the range of 700−1600 cm^{-1} are those of 2-methylimidazole ligands, and the stretching vibration peak of the C = N bond in the imidazole ring appears at 1584 cm^{-1}, indicating that organic ligands were not lost due to Fe doping(Sun et al. 2020). The XRD analysis was also verified, indicating that the introduction of Fe did not affect the structure of ZIF-8. And its abundant functional groups, such as C-H, C = N, and Zn-N, provide abundant active sites for adsorption.

3.1.4 BET analysis

Figure S1(a), (b), and (c) depict the N_2 adsorption-desorption isotherms for ZIF-8 and FZM, demonstrating that ZIF-8 and FZM have type I and IV isotherms, as well as type H1 and H4 hysteresis loops, respectively(Li et al. 2019). In addition, the hysteresis loops are in the 0.45 < P/P_0 < 1.0 range, indicating that FZM has a hierarchical porous structure with micropores and mesopores. Compared with pristine ZIF-8 (983.44 m²/g), FZM (1110.39 m²/g) has a higher specific surface area. In addition, the pore volume of FZM was 0.521 cm^3/g, which was increased compared with 0.443 cm^3/g of ZIF-8, and the average pore size decreased from 6.30 nm of ZIF-8 to 5.81 nm of FZM, indicating that after the addition of Fe and MWCNTs, the pore structure changes significantly, yet has little effect on the formation of pristine ZIF-8.

Moreover, the reduced pore size can provide more active sites for the attachment of pollutants, which can effectively improve the performance of the adsorbent.

3.1.5 TG analysis

TGA thermogravimetric analysis curves of two distinct adsorbents in the N_2 atmosphere at 800°C are shown in Figure S1(d). The figure clearly shows that both adsorbents are thermally stable. Both adsorbents lost weight at 550°C, 7.62% for ZIF-8 and 11.11% for FZM, respectively, due to water and organic solvent, as well as the unreacted 2-methylimidazole. When the temperature approached 600°C, the weight of both adsorbents dropped dramatically, owing to the fracture and skeletal collapse of Fe-N or Zn-N. Both adsorbents have good thermal stability within 550°C, similar to that previously reported for ZIF-8, however, FZM has a lower heat resistance temperature than ZIF-8(Wu et al. 2015).

3.1.6 XPS analysis

XPS was used to scrutinize the surface chemical composition of FZM, and the results are displayed in Figure S2. The observed scanning spectrum of FZM is depicted in Figure S2(a), indicating that the composite material is mostly composed of elements including C, N, Fe, and Zn. The presence of Fe implies that the metal-organic framework has been successfully doped with Fe. As shown in Figure S2(b), C 1s is divided into two peaks, with C = C/C-C and C-N/C-H. N 1s is similarly divided into two peaks in Figure S2(c), pyridine N and Fe-N/Zn-N; the existence of Fe-N confirms the successful synthesis of Fe-ZIF-8(Yang et al. 2021). Figure S2(d) reveals that $2p_{3/2}$ and $2p_{1/2}$, which are positioned at 1021.8 eV and 1044.8 eV, respectively, contribute the majority of the Zn 2p spectrum, confirming that the introduction of Fe did not affect the normal synthesis of the ZIF-8 framework. The peaks of Fe element in Figure S2(e) comprise Fe^{2+} $2p^{3/2}$ (710.58 eV), Fe^{3+} $2p^{3/2}$ (713.13 eV), Fe^{2+} $2p^{1/2}$ (723.43 eV), and Fe^{3+} $2p^{1/2}$ (727.86 eV) owing to the addition of Fe^{2+} element. The existence of Fe^{3+} may be attributed to Fe^{2+} being exposed to air and oxidized to Fe^{3+} during the material fabrication.

3.2 Adsorption performance

3.2.1 Effects of iron doping, adsorbent dosage

Figure S3(a) illustrates the effect of ZIF-8, MWCNTs, and three ZIF-8/MWCNTs with varying Fe doping quantities on the adsorption capacity of TC at an initial concentration of 100mg/L, 298K, and pH = 6 for 6 hours. When the amount of Fe doping was raised from 0 mg to 150 mg, the adsorption capacity of TC increased from 321.7 mg/g to 416.1 mg/g, then reduced to 364.8 mg/g, suggesting that Fe doping improved the adsorption performance of ZIF-8. When the amount of doping was increased, however, the adsorption effect diminished. The doping concentration may be too high, triggering a partial collapse of the metal-organic skeleton structure and hence a reduction in adsorption performance. Furthermore, the addition of MWCNTs significantly increased the adsorption capacity of TC, demonstrating that the addition of MWCNTs also promoted the material's adsorption performance.

Figure S3(b) depicts the effect of FZM dosing on the adsorption capacity of TC at a TC concentration of 100 mg/L at 298 K and pH = 6. The removal rate of TC increased from 31.19−55.11% as the FZM dosage was increased from 50 mg/L to 250 mg/L, whereas adsorption capacity declined by roughly 65% from 623.8 mg/g to 220.44 mg/g. The increase in TC removal could be attributable to a higher adsorbent dosage, which offered underutilized adsorption sites, resulting in a considerable reduction in adsorption capacity(Yu & Wu 2020). The ideal dosage of adsorbent is determined to be 100mg/L based on a cost-benefit assessment of price and adsorption effect.

3.2.2 Effect of pH

The pH of the solution is also crucial in the adsorption process. Under the conditions of 100 mg/L TC initial concentration, 100 mg/L FZM dose, and 298 K temperature, the effect of pH value on TC adsorption capacity on FZM was investigated in this work. Figure 3 depicts the results.

Figure 3 demonstrates that as the pH of the solution increased from 2 to 6, the adsorption capacity of FZM for TC increased. When the pH was raised from 6 to 12, the adsorption capacity decreased considerably. It shows that the capability of TC adsorption on FZM is pH-dependent. The adsorption capacity of TC increases at first and then declines as the pH of the solution rises. TC has cationic species TC^+ (pH<3.3), oligomeric ionic species TC^0 (3.3−/TC^{2-} (pH > 7.8) ionic states, according to previous research(Wang et al. 2020). When the pH<3.3, TC exists in the form of TC^+, and a huge number of positive charges accumulate on the surface of FZM, resulting in the obvious electrostatic repulsion between the adsorbent and TC^+. When the pH is between 3.3 and 7.8, the proton concentration in the solution decreases, lowering the positive charge on the adsorbent FZM's surface, and TC exists in the form of TC^0, weakening the electrostatic repulsion between the two and increasing the adsorption capacity. When the pH⬚7.8, TC molecules exist in the form of anionic species TC^-/TC^{2-}, and the OH^- content in the solution gradually increases, resulting in the accumulation of negative charges on the FZM's surface, and the adsorbent and anions generate electrostatic repulsion, obstructing the contact between the TC and the FZM surface, lowering the adsorption capacity. Therefore, electrostatic interaction is critical in the process of TC adsorption on FZM.

3.2.3 Effect of ionic strength

Since TC commonly coexists with other ions in natural waters, and these ions can promote or inhibit TC's adsorption effect, the effect of coexisting ions must be investigated. As a consequence, at concentrations of 50 and 100 mg/L, this experiment explored the effects of five typically found in water compounds, such as NaCl, Na_2SO_4, Na_2CO_3, $MgCl_2$, and $CaCl_2$, on TC adsorption by FZM. The TC adsorption experiment was carried out using separate 50 and 100 mg/L coexisting ionic precursors, and after the reaction was completed for 6 hours, the TC concentration in the residual solution was measured and the TC adsorption capacity was calculated.

As shown in Figure S4, the adsorption of TC by FZM was significantly inhibited in the presence of NaCl, Na_2SO_4, Na_2CO_3, and $MgCl_2$, and the inhibition increased as the ion concentration increased from 50

mg/L to 100 mg/L. This indicates that these ions have a competitive effect on the adsorption of TC on FZM, probably Cl^-, SO_4^{2-}, and Mg^{2+} occupy the adsorption sites on the adsorbent surface, resulting in the hindrance of TC contact with the adsorbent. The hydrolysis of CO_3^{2-} to create OH^-, which makes the solution alkaline and hence affects the solution pH during adsorption, might explain the reduction in TC adsorption capacity in the presence of CO_3^{2-}. However, in the presence of Ca^{2+}, the adsorption of TC by FZM was promoted and the TC adsorption capacity increased instead, but when the concentration of Ca^{2+} was increased to 100 mg/L, the TC adsorption capacity decreased compared to that at 50 mg/L, but it was still higher than that without Ca^{2+} addition.

3.3 Adsorption modeling

3.3.1 Adsorption kinetics

Figure 4(a) depicts the effect of increasing the reaction time on the adsorption capacity of TC by FZM under the following conditions: TC concentration of 100 mg/L, 298K, and pH = 6. Figure 8(a) shows that as time passes, the adsorption capacity increases rapidly, then slows down before reaching equilibrium at 420 min. The adsorption capacity rises rapidly because there are adequate adsorption sites on the adsorbent's surface. The number of adsorption sites decreases as reaction time increases, rendering TC adsorption harder and driving the TC adsorption capacity to plateau(Tang et al. 2021).

Pseudo-first-order (PFO), pseudo-second-order (PSO), and intra-particle diffusion (ID) kinetic models were used to investigate the experimental data of FZM adsorption of TC, to predict the potential rate control steps of adsorption, and understand the adsorption mechanism deeply. Figure 4 and Table S2 demonstrate the linear fitting curves of the experimental data of TC adsorption through three adsorption kinetic models, as well as the corresponding model parameters. Table 4 shows that the PSO model's correlation coefficient (R^2) value ($R^2 = 0.986$) is substantially closer to one, indicating that it is the best fit for the experimental data of TC adsorption by FZM. Chemical adsorption may be the rate-determining step and controlling factor in the TC adsorption process, according to the PSO model's hypothesis(Tang et al. 2021). Although Q_t and $t^{0.5}$ in the ID model have a good linear correlation, the fitted straight line in the figure does not pass through the origin, indicating that the ID model is not the only rate-limiting step. According to the foregoing, chemical adsorption may be the rate-determining step and controlling factor in the TC adsorption process on FZM.

3.3.2 Adsorption isotherms

For TC adsorption on FZM, the primary concentration of TC is also an essential factor. The influence of varying initial TC concentrations in the range of 10-100mg/L on adsorption capacity was examined using FZM in this research. Figure 5(a) depicts the change in adsorption capacity as TC concentrations increase. TC adsorption capacity was steadily enhanced by FZM from 10 to 100 mg/L. This demonstrates that the surface of FZM has enough adsorption sites for TC adsorption. As a result, for subsequent study, the TC concentration recommended is 100 mg/L.

Some conventional adsorption isotherm models were employed to fit the data of the effect of the initial concentration of TC on the adsorption capacity to further explain the removal mechanism of TC by FZM. The adsorption capacity increased significantly with the TC concentration increased under the conditions of a temperature of 298 K and the solution pH of 6, and the adsorption capacity reached its maximum at the 100-mg/L solution of TC, as shown in Fig. 5(a).

Figure 5(b), (c), and (d) depict the adsorption data for three different TC adsorption isotherms on FZM, while Table S3 lists the model parameters. When the correlation coefficients(R^2) of the three adsorption isotherms are compared, it can be determined that the Freundlich model's R^2 is 0.998 closest to 1, revealing that the Freundlich isotherm can describe the TC removal process on FZM best. TC adsorption on FZM's surface occurs as multilayer adsorption, according to the assumptions of the Freundlich model. Furthermore, the maximum saturation adsorption capacity fitted to the Langmuir model was 1111.11 mg/g, which was superior to several other materials previously reported for the removal of TC from water (as listed in Table 1), showing that the FZM material as-synthesized in this study has a greater potential for TC removal from water.

Table 1
Comparison of the adsorption performance of various adsorbents on TC.

Adsorbents	Temperature (K)	Equilibrium time (min)	pH	Q_{max} (mg/g)	References
Graphene oxide	298	90	3.6	313	(Gao et al. 2012)
Rice straw derived biochar	298	120	2–11	98.33	(Dai et al. 2020)
Magnetic graphene oxide	298	10	3–10	39.1	(Lin et al. 2013)
PDA-NFsM	298	60	3–10	142.9	(Jian et al. 2021)
NH_2-MIL-101(Fe)	298	120	7.0	378	(Dong et al. 2020)
FZM	298	480	6.0	1111.11	This study

3.3.3 Adsorption thermodynamics

Temperature is another major component that influences TC adsorption on FZM in wastewater. At a TC concentration of 100 mg/L, pH value of 6, and adsorbent dose of 100 mg/L, the fluctuation of TC

adsorption capability at different temperature settings (298K, 308K, 318K) was examined independently in this work.

The values of ΔG^0 obtained at all three temperatures are negative, showing that the adsorption of TC on FZM occurs spontaneously, as shown in Table 2. Furthermore, the adsorption process's ΔH^0 value becomes positive, indicating that the reaction is heat-absorbing, that TC adsorption capacity increases with increasing temperature, and that high temperatures are advantageous for boosting TC adsorption. Additionally, ΔS^0 is greater than 0, implying that the adsorbent has a stronger affinity for TC molecules.

Table 2
Thermodynamic parameters of adsorption of TC on FZM.

Adsorbent	Temperature(K)	ΔG^0 (KJ/mol)	ΔH^0 (KJ/mol)	ΔS^0 (J/mol/K)
FZM	298.15	-4.823	12.650	0.059
	308.15	-5.409		
	318.15	-5.995		

3.4 Possible adsorption mechanism

The mechanism of TC adsorption by FZM was investigated in-depth to appropriately improve the current adsorbent and manufacture a higher performance adsorbent material. The findings of the FTIR characterization examination of the FZM materials before and after TC adsorption are presented in Fig. 6.

The FZM diffraction peaks after TC adsorption are nearly identical to those before adsorption, implying that the structure of the fabricated FZM composites remains stable during the adsorption process. Compared with the FZM before adsorption, the FZM after TC adsorption shows a fresh characteristic peak at 1258 cm^{-1}, which is caused by the stretching vibration of the -CH$_3$ group on the benzene ring in the TC molecule. Moreover, the intensity of the characteristic peak at 1591 cm^{-1} is significantly enhanced and red-shifted, which could be owing to the TC molecule's absorption of the N-H deformation vibration(Gao et al. 2012). Moreover, a broad peak appears, and the characteristic peak's intensity is significantly enhanced at 3200−3500 cm^{-1}. This is probably due to the stretching vibration of intermolecular hydrogen bonds, indicating that the -OH on TC is adsorbed on the FZM's surface by hydrogen bonding(Ma et al. 2020). Meanwhile, the development of a new distinctive peak at 592 cm^{-1}, considered to be formed by Fe-O stretching, indicates that Fe on the surface of FZM has complexed with the oxygen-containing functional groups in TC molecules and that TC molecules have been bound to FZM by Fe-O. It also demonstrates that Fe doping introduces additional active sites for TC adsorption, resulting in FZM having a greater adsorption capacity on TC than virgin ZIF-8(Gu et al. 2021). No new

distinctive peak was discovered at 423 cm^{-1}, showing that Zn is not engaged in the TC adsorption process. Furthermore, it was discovered that there is an electrostatic connection between FZM and TC molecules, and the FZM surface is positively charged, in a research on the effect of pH on the adsorption of TC by FZM. Additionally, because of the π-π interactions between TC molecules and the metal-organic backbone material, FZM still has a high adsorption capacity for TC molecules at high pH(Xiong et al. 2018). In summary, different adsorption interactions such as H bonding, surface complexation, π-π interactions, and electrostatic interactions are involved in the adsorption of TC on FZM composites, and the possible mechanism diagram is shown in Fig. 7.

3.6 RSM Optimization

Three models in BBD were employed to explore the relationships between the adsorption capacity of TC and pH, temperature, and adsorbent dosage. The quadratic polynomial model fits the data better.

As stated in Eq. 3.1, a quadratic polynomial between the response variable Y (adsorption capacity) and the independent variables A (pH), B (temperature), and C (dosage) was constructed based on the results of the quadratic polynomial model fitting.

$$Y=537.78-13.26A+28.28B-114.19C-7.83AB-12.60AC$$

$$+2.62BC-102.24A^2-34.37B^2+22.91C^2 \ (3.1)$$

Where Y represents the adsorption capability of TC, A represents solution pH, B represents system temperature, and C represents adsorbent dosage.

The equation shows that increasing the pH and adsorbent dosage amount inhibits the increase of TC adsorption capacity, but increasing the temperature promotes the increase of adsorption capacity. In comparison to the other two independent variables, the coefficient of adsorbent dosage was found to be the largest, indicating that the amount of dosing had the greatest effect on the change in TC adsorption capacity. Adsorbent dosage > pH > temperature were the independent variables impacting TC's adsorption ability in that order.

To elucidate these effects, an analysis of variance (ANOVA) on the data was required. The results of the ANOVA for the quadratic model obtained from the BBD are presented in Table 3. From the interpretation of the model fit parameters, we can obtain that the bigger the F-value and the smaller the p-value, the more significant the model is. As can be seen from the table, an F-value of 229.68 for the model implies that this model is statistically significant and a p-value less than 0.05 indicates that the model term is significant, so the model can be used to explain the statistical results of the adsorption capacity of TC on FZM and to predict the optimal conditions. The individual factors pH (A), temperature (B), and dosage (C), as well as the interaction terms AC, A^2, B^2, and C^2, had p-values less than 0.05, indicating that all of the above variables were significant model terms.

Table 3
ANOVA analysis results of BBD model for adsorption of TC on FZM.

Source	Sum of squares	df	Mean square	F-value	p-value
Model	163800.00	9	18203.39	229.68	< 0.0001
A-pH	1407.15	1	1407.15	17.75	0.004
B-Temperature	6395.8	1	6395.80	80.70	< 0.0001
C-Dosage	104300	1	104300.00	1316.12	< 0.0001
AB	244.92	1	244.92	3.09	0.1222
AC	635.04	1	635.04	8.01	0.0254
BC	27.56	1	27.56	0.3478	0.5739
A^2	43155.95	1	43155.95	544.51	< 0.0001
B^2	4972.43	1	4972.43	62.74	< 0.0001
C^2	2209.97	1	2209.97	27.88	0.0011
Residual	554.79	7	79.26		
Lack of Fit	455.74	3	151.91	6.13	0.0561
Pure Error	99.05	4	24.76		
Cor Total	164400.00	16			
Std. Dev.	8.90		R^2	0.9966	
Mean	484.75		Adjusted R^2	0.9923	
C.V. %	1.84		Predicted R^2	0.9547	
			Adeq precision	50.7857	

Adequate precision (AP), Coefficient of variance (C.V.%), Standard deviation (Std. Dev.), and Regression coefficient (R^2) were used to assess the reliability and accuracy of the experimental response (R^2). The AP value was larger than 4.0, and the C.V. % value was 1.84, indicating that the experimental data was reliable. The "adjusted R^2" and "predicted R^2," respectively, are 0.9923 and 0.9547, with a difference of less than 0.2, showing that the experimental data are well matched for the quadratic model. Meanwhile, the R^2 value for the TC adsorption model is 0.9966, which implies a linear correlation between the actual experimental response and the projected TC response, indicating that this experimental model is reliable and applicable. Thus, these results reconfirm that the proposed adsorption optimization model for TC on FZM is statistically significant and can be used to predict the optimal conditions.

To validate the model, comparative and diagnostic plots were obtained in addition to these statistics. The residuals are the differences between the model and experimental values, and the degree of model fit is determined by the model's position and the experimental data. Figure S5(a) further shows that the TC adsorption model's real reaction has a good linear correlation with the predicted response, showing that the actual TC adsorption capacity values are in good accord with the model predictions. Figure S5(b) also shows the model's residual plots, which are used to confirm the extent of the model's fit. Therefore, the model prediction for TC adsorption on FZM is acceptable.

Over a range of specified variables, the effects of pH-temperature, temperature-dosage, and pH-dosage on the adsorption of TC on FZM were determined, and the results are depicted as three-dimensional surface plots and contours. The effects of pH-temperature, pH-dosing amount, and temperature-dosing amount on the adsorption capacity of TC on FZM are shown in Figure 8 (a) and (b), (c) and (d), and (e) and (f), respectively. The optimal conditions for TC adsorption on FZM, according to the model, were pH 7.1, temperature 312.5 K, and injection amount 64.43 mg/L. 599.78 mg/g was the maximum capacity prediction point for TC. Experiments were conducted under the optimal conditions predicted by the model to verify the accuracy and reliability of the model, and the results showed that the adsorption capacity of FZM on TC under these conditions was 589.42 mg/g, with a 1.73 % deviation between them. This reveals that utilizing RSM to optimize TC adsorption by FZM is effective, and RSM may be used to determine the best adsorption experimental conditions.

3.7 Reusability of FZM

The adsorbent's recoverability is a critical component in determining its economics and practical applicability. FZM was introduced to a centrifuge tube containing 50 mL of TC solution at a dosage of 100 mg/L, and the tube was then placed in a thermostatic shaker at 298 k and 160 rpm for 240 min at a 100-mg/L TC and a pH of 6. The adsorbent was washed three times with 0.1M NaOH and ultrapure water alternately, then dried in vacuum at 60°C for 12 h. The reuse performance of FZM was investigated through four cycles of regeneration tests, the results of which are presented in Fig. 9. The results revealed that FZM's adsorption capacity on TC declined significantly after four cycles, but it still exceeded 370 mg/g, confirming that FZM's adsorption performance remained good after four regenerations. It suggests that FZM has excellent reusability in the TC removal process and has the potential to be utilized in application development.

3.8 Production Cost Estimation

The low yield of metal-organic framework materials is one of their drawbacks, which leads to high production costs and limits the materials' mass production and practical applications. As a result, we calculated the manufacturing cost of the MFZ composites used in this study, to determine the components of production cost and the percentage of each component, as well as analyze and explore cost-cutting alternatives. The cost of MFZ preparation is mostly comprised of the cost of raw ingredients (cost A), cleaning solvents (cost B), power, tap water, and ultrapure water (cost C). Based on the existing

laboratory scale and the bulk purchase price of materials on the market, a simple estimate of these expenditures was made. Cost A is estimated to be US$59.45/kg, cost B is estimated to be US$150.46/kg, and cost C is estimated to be US$0.60/kg, making a total cost of US$210.51 to generate 1 kg of FZM composite. According to the response surface optimization results, the adsorption capacity attained under the projected optimal conditions is 589.42 mg/g, costing US$0.36 per gram of TC adsorbed.

Additionally, as shown above, the cleaning solvent accounts for up to 71% of the whole cost. The cleaning solvent is usually used only once in the laboratory preparation process; however, in large-scale production, the cleaning solvent is recycled to some extent, typically up to 90%(Luo et al. 2021). As a result, the total cost would be 75.10 US$/kg. At the current time, the cost of treating 100 mg/L of TC wastewater at a dosage of 64.43 mg/L is around US$4.84/m^3. Furthermore, repeated regeneration trials with FZM composites have revealed that FZM has good reusability and may be recycled and reused, lowering the cost of usage even further.

4. Conclusions

A simple precipitation approach and a solvothermal method were used to successfully synthesize Fe-doped ZIF-8 loaded multi-walled carbon nanotubes in this research. The prepared adsorbent was utilized to investigate TC adsorption performance and mechanism in wastewater. The pseudo-first-order kinetic and Freundlich isotherm models fit the adsorption experimental data the best, demonstrating that the adsorption of TC by FZM is multilayer adsorption with chemisorption as the rate-limiting step in the adsorption process. The Langmuir model was used to fit the theoretical maximum saturation adsorption capacity of 1111.11 mg/g, which was better than other adsorbents. Furthermore, the TC adsorption on FZM is a heat-absorbing and spontaneous process. Possible TC adsorption methods on FZM include hydrogen bonding between FZM and TC molecules, surface complexation, π-π interactions, and electrostatic interactions. The projected adsorption capacity of TC was 599.78 mg/g under optimal adsorption circumstances of pH 7.1, temperature 312.5 K, and dosage amount 64.43 mg/L, with a 1.73% divergence from the actual result, according to response surface optimization trials. FZM displayed good reusability for TC adsorption, according to the results of the four-cycle experiment. For treating 100 mg/L of TC effluent, the production cost estimate came in at around US$8.35/m^3. In conclusion, FZM demonstrated exceptional TC removal effectiveness and recyclability, indicating the considerable potential for practical application.

Declarations

Author Contribution

Jiacheng Li: Writing - review & editing. **Tian Tian** & **Yannan Jia:** Data curation. **Nannan Xu** & **Shujun Yang:** Conceptualization, Methodology, Supervision. **Chenyue Zhang, Shiwei Gao** & **Wei Shen:** Data curation. **Zheng Wang:** Conceptualization, Methodology, Supervision.

Data availability The data is true and reliable

Ethical approval Not applicable.

Consent to participate All authors agree to participate in the editing of the paper.

Consent for publication All authors agree to publish this manuscript in your journal.

Conflict of interest The authors declare no competing interests

References

1. Akbari MZ, Xu YF, Lu ZK, Peng L (2021) Review of antibiotics treatment by advance oxidation processes. Environmental Advances 5:100111. https://doi.org/10.1016/j.envadv.2021.100111

2. Ashworth DJ, Ibekwe AM (2020) System of multi-layered environmental media for the removal of antibiotics from wastewater. Journal of Environmental Chemical Engineering 8(5):104206. https://doi.org/10.1016/j.jece.2020.104206

3. Bao J, Zhu YZ, Yuan SJ, Wang FH, Tang H, Bao ZH, Zhou HY, Chen YJ (2018) Adsorption of tetracycline with reduced graphene oxide decorated with $MnFe_2O_4$ nanoparticles. Nanoscale Research Letters 13(1):396. https://doi.org/10.1186/s11671-018-2814-9

4. Brinzila CI, Pacheco MJ, Ciríaco L, Ciobanu RC, Lopes A (2012) Electrodegradation of tetracycline on BDD anode. Chemical Engineering Journal 209:54-61. https://doi.org/10.1016/j.cej.2012.07.112

5. Chen S, Jiang SF, Jiang H (2020) A review on conversion of crayfish-shell derivatives to functional materials and their environmental applications. Journal of Bioresources and Bioproducts 5(4):238-247. https://doi.org/10.1016/j.jobab.2020.10.002

6. Dai JW, Meng XF, Zhang YH, Huang YJ (2020) Effects of modification and magnetization of rice straw derived biochar on adsorption of tetracycline from water. Bioresource Technology 311(123455. https://doi.org/10.1016/j.biortech.2020.123455

7. Ding Y, Xu YF, Ding B, Li Z, Xie FZ, Zhang FJ, Wang HT, Liu J, Wang XB (2017) Structure induced selective adsorption performance of ZIF-8 nanocrystals in water. Colloids and Surfaces A: Physicochemical and Engineering Aspects 520:661-667. https://doi.org/10.1016/j.colsurfa.2017.02.012

8. Dong YN, Hu TD, Pudukudy M, Su HY, Jiang LH, Shan SY, Jia QM (2020) Influence of microwave-assisted synthesis on the structural and textural properties of mesoporous MIL-101(Fe) and NH_2-MIL-101(Fe) for enhanced tetracycline adsorption. Materials Chemistry and Physics 251:123060. https://doi.org/10.1016/j.matchemphys.2020.123060

9. Fei HH, Cahill JF, Prather KA, Cohen SM (2013) Tandem postsynthetic metal ion and ligand exchange in zeolitic imidazolate frameworks. Inorganic Chemistry 52(7):4011-4016. https://doi.org/10.1021/ic400048g

10. Feng YX, Zhong L, Hou Y, Jia SR, Cui JD (2019) Acid-resistant enzyme@MOF nanocomposites with mesoporous silica shells for enzymatic applications in acidic environments. Journal of Biotechnology 306:54-61. https://doi.org/10.1016/j.jbiotec.2019.09.010

11. Gao Y, Li Y, Zhang L, Huang H, Hu JJ, Shah SM, Su XG (2012) Adsorption and removal of tetracycline antibiotics from aqueous solution by graphene oxide. Journal of Colloid and Interface Science 368(1):540-546. https://doi.org/10.1016/j.jcis.2011.11.015

12. Gu WY, Huang XY, Tian YH, Cao M, Zhou, Zhou Y, Lu J, Lei JY, Zhou YB, Wang LZ, Liu YD, Zhang JL (2021) High-efficiency adsorption of tetracycline by cooperation of carbon and iron in a magnetic Fe/porous carbon hybrid with effective Fenton regeneration. Applied Surface Science 538:147813. https://doi.org/10.1016/j.apsusc.2020.147813

13. Huang XC, Zhang XY, Feng FX, Xu XP (2014) Biodegradation of tetracycline by the yeast strain *Trichosporon mycotoxinivorans* XPY-10. Preparative Biochemistry and Biotechnology 46(1):15-22. https://doi.org/10.1080/10826068.2014.970692

14. Huang ZA, Zhou JQ, Zhao YY, Cheng HB, Lu GX, Morawski AW, Yu Y (2021) Stable core−shell ZIF-8@ZIF-67 MOFs photocatalyst for highly efficient degradation of organic pollutant and hydrogen evolution. Journal of Materials Research 36(3):602-614. https://doi.org/10.1557/s43578-021-00117-5

15. Jian NG, Dai YY, Wang YL, Qi FF, Li SJ, Wu YJ (2021) Preparation of polydopamine nanofibers mat as a recyclable and efficient adsorbent for simultaneous adsorption of multiple tetracyclines in water. Journal of Cleaner Production 320:128875. https://doi.org/10.1016/j.jclepro.2021.128875

16. Li B, Huang YY, Wang ZX, Li JL, Liu Z, Fan SS (2021) Enhanced adsorption capacity of tetracycline on tea waste biochar with $KHCO_3$ activation from aqueous solution. Environmental Science and Pollution Research 28(32):44140-44151. https://doi.org/10.1007/s11356-021-13817-6

17. Li J, Wu Z, Duan QY, Li XD, Tan XL, Alsaedi A, Hayat T, Chen CL (2019) Mutual effects behind the simultaneous U(VI) and humic acid adsorption by hierarchical MWCNT/ZIF-8 composites. Journal of Molecular Liquids 288:110971. https://doi.org/10.1016/j.molliq.2019.110971

18. Li K, Li JJ, Zhao N, Ma Y, Di B (2020) Removal of tetracycline in sewage and dairy products with high-stable MOF. Molecules 25(6):1312. https://doi.org/10.3390/molecules25061312

19. Lin YX, Xu S, Li J (2013) Fast and highly efficient tetracyclines removal from environmental waters by graphene oxide functionalized magnetic particles. Chemical Engineering Journal 225:679-685. https://doi.org/10.1016/j.cej.2013.03.104

20. Liu H, Yang YK, Sun HF, Zhao L, Liu Y (2018) Fate of tetracycline in enhanced biological nutrient removal process. Chemosphere 193:998-1003. https://doi.org/10.1016/j.chemosphere.2017.11.136

21. Liu YN, Li FM, Deng JQ, Wu ZQ, Lei TZ, Tan MJ, Wu ZJ, Qin XL, Li H (2021) Mechanism of sulfamic acid modified biochar for highly efficient removal of tetracycline. Journal of Analytical and Applied

Pyrolysis 158:105247. https://doi.org/10.1016/j.jaap.2021.105247

22. Luo HX, Cheng FW, Huelsenbeck L, Smith N (2021) Comparison between conventional solvothermal and aqueous solution-based production of UiO-66-NH$_2$: Life cycle assessment, techno-economic assessment, and implications for CO$_2$ capture and storage. Journal of Environmental Chemical Engineering 9(2):105159. https://doi.org/10.1016/j.jece.2021.105159

23. Ma J, Xiong YC, Dai XH, Yu F (2020) Coadsorption behavior and mechanism of ciprofloxacin and Cu(II) on graphene hydrogel wetted surface. Chemical Engineering Journal 380:122387. https://doi.org/10.1016/j.cej.2019.122387

24. Minale M, Gu ZL, Guadie A, Kabtamu DM, Li Y, Wang XJ (2020a) Application of graphene-based materials for removal of tetracyclines using adsorption and photocatalytic-degradation: A review. Journal of Environmental Management 276:111310. https://doi.org/10.1016/j.jenvman.2020.111310

25. Nagarjun N, Dhakshinamoorthy A (2019) A Cu-Doped ZIF-8 metal organic framework as a heterogeneous solid catalyst for aerobic oxidation of benzylic hydrocarbons. New Journal of Chemistry 43(47):18702-18712. https://doi.org/10.1039/C9NJ03698A

26. Nasseri S, Mahvi AH, Seyedsalehi M, Yaghmaeian K, Nabizadeh R, Alimohammadi M, Safari GH (2017) Degradation kinetics of tetracycline in aqueous solutions using peroxydisulfate activated by ultrasound irradiation: Effect of radical scavenger and water matrix. Journal of Molecular Liquids 241:704-714. https://doi.org/10.1016/j.molliq.2017.05.137

27. Norvill ZN, Toledo-Cervantes A, Blanco S, Shilton A, Guieysse B, Muñoz R (2017) Photodegradation and sorption govern tetracycline removal during wastewater treatment in algal ponds. Bioresource Technology 232:35-43. https://doi.org/10.1016/j.biortech.2017.02.011

28. Pei JY, Chen ZS, Wang YQ, Xiao B, Zhang ZB, Cao XH, Liu YH (2022) Preparation of phosphorylated iron-doped ZIF-8 and their adsorption application for U(VI). Journal of Solid State Chemistry 305(122650. https://doi.org/10.1016/j.jssc.2021.122650

29. Sun SW, Yang ZH, Cao J, Wang Y, Xiong WP (2020) Copper-doped ZIF-8 with high adsorption performance for removal of tetracycline from aqueous solution. Journal of Solid State Chemistry 285:121219. https://doi.org/10.1016/j.jssc.2020.121219

30. Tang XH, Huang YY, He Q, Wang YJ, Zheng HL, Hu YD (2021) Adsorption of tetracycline antibiotics by nitrilotriacetic acid modified magnetic chitosan-based microspheres from aqueous solutions. Environmental Technology & Innovation 24:101895. https://doi.org/10.1016/j.eti.2021.101895

31. Tsai CW, Kroon RE, Swart HC, Terblans JJ, Harris RA (2019) Photoluminescence of metal-imidazolate complexes with Cd(II), Zn(II), Co(II) and Ni(II) cation nodes and 2-methylimidazole organic linker. Journal of Luminescence 207:454-459. https://doi.org/10.1016/j.jlumin.2018.11.026

32. Vo TK, Kim JS (2021) Facile synthesis of magnetic framework composite MgFe$_2$O$_4$@UiO-66(Zr) and its applications in the adsorption−photocatalytic degradation of tetracycline. Environmental Science and Pollution Research 28(48):68261-68275. https://doi.org/10.1007/s11356-021-15423-y

33. Wang NY, Liu Y, Qiao ZW, Diestel L, Zhou J, Huang AS, Caro J (2015) Polydopamine-based synthesis of a zeolite imidazolate framework ZIF-100 membrane with high H_2/CO_2 selectivity. Journal of Materials Chemistry A 3(8):4722-4728. https://doi.org/10.1039/c4ta06763k

34. Wang SL, Ji B, Zhang M, Gu J, Ma YQ, Liu Y (2021) Tetracycline-induced decoupling of symbiosis in microalgal-bacterial granular sludge. Environmental Research 197:111095. https://doi.org/10.1016/j.envres.2021.111095

35. Wang W, Gao M, Cao MB, Liu X, Yang HB, Li YS (2021) A series of novel carbohydrate-based carbon adsorbents were synthesized by self-propagating combustion for tetracycline removal. Bioresource Technology 332:125059. 10.1016/j.biortech.2021.125059

36. Wang YF, Zhao W, Qi ZY, Zhang L, Zhang YN, Huang HO, Peng YZ (2020) Designing ZIF-8/hydroxylated MWCNT nanocomposites for phosphate adsorption from water: Capability and mechanism. Chemical Engineering Journal 394:124992. https://doi.org/10.1016/j.cej.2020.124992

37. Wang ZL, Chen XY, Meng Z, Zhao MX, Zhan HJ, Liu WY (2020) A water resistance magnetic graphene-anchored zeolitic imidazolate framework for efficient adsorption and removal of residual tetracyclines in wastewater. Water Science and Technology 81(11):2322-2336. https://doi.org/10.2166/wst.2020.283

38. Wei W, Liu J, Jiang JW (2020) Atomistic simulation study of polyarylate/zeolitic-imidazolate framework mixed-matrix membranes for water desalination. ACS Applied Nano Materials 3(10):10022-10031. https://doi.org/10.1021/acsanm.0c02004

39. Wu CS, Xiong ZH, Li C, Zhang JM (2015) Zeolitic imidazolate metal organic framework ZIF-8 with ultra-high adsorption capacity bound tetracycline in aqueous solution. RSC advances 5(100):82127-82137. https://doi.org/10.1039/C5RA15497A

40. Xiong WP, Zeng GM, Yang ZH, Zhou YY, Zhang C, Cheng M, Liu Y, Hu L, Wan J, Zhou CY, Xu R, Li X (2018) Adsorption of tetracycline antibiotics from aqueous solutions on nanocomposite multi-walled carbon nanotube functionalized MIL-53(Fe) as new adsorbent. Science of The Total Environment 627:235-244. https://doi.org/10.1016/j.scitotenv.2018.01.249

41. Yang H, Hu S, Zhao H, Luo XF, Liu Y, Deng CF, Yu YL, Hu TD, Shan SY, Zhi YF, Su HY, Jiang LH (2021) High-performance Fe-doped ZIF-8 adsorbent for capturing tetracycline from aqueous solution. Journal of Hazardous Materials 416:126046. https://doi.org/10.1016/j.jhazmat.2021.126046

42. Yaqubi O, Tai MH, Mitra D, Gerente C, Neoh KG, Wang CH, Andres Y (2021) Adsorptive removal of tetracycline and amoxicillin from aqueous solution by leached carbon black waste and chitosan-carbon composite beads. Journal of Environmental Chemical Engineering 9(1):104988. https://doi.org/10.1016/j.jece.2020.104988

43. Yu RB, Wu ZC (2020) High adsorption for ofloxacin and reusability by the use of ZIF-8 for wastewater treatment. Microporous and Mesoporous Materials 308:110494. https://doi.org/10.1016/j.micromeso.2020.110494

44. Zhang DL, Zhang JH, Pan MD, Wang Y, Sun T (2021) Necklace-like C-ZIF-8@MWCNTs fabricated by electrochemical deposition towards enhanced supercapacitor. Journal of Alloys and Compounds

853:157368. https://doi.org/10.1016/j.jallcom.2020.157368

45. Zhang LY, Xin ZW, Fei XY, Luo HY, Li HY, Lu BX, Li ZM, Wei GT (2019) Study on adsorption of tetracycline by red mud-based ceramsite. Journal of Water Supply: Research and Technology-Aqua 68(1):39-50. https://doi.org/10.2166/aqua.2018.100

46. Zhao YP, Geng JJ, Wang XR, Gu XY, Gao SX (2011) Tetracycline adsorption on kaolinite: pH, metal cations and humic acid effects. Ecotoxicology 20(5):1141-1147. https://doi.org/10.1007/s10646-011-0665-6

47. Zhou QQ, Liu GJ, Arif M, Shi XD, Wang SZ (2021) Occurrence and risk assessment of antibiotics in the surface water of Chaohu Lake and its tributaries in China. Science of The Total Environment 807:151040. https://doi.org/10.1016/j.scitotenv.2021.151040
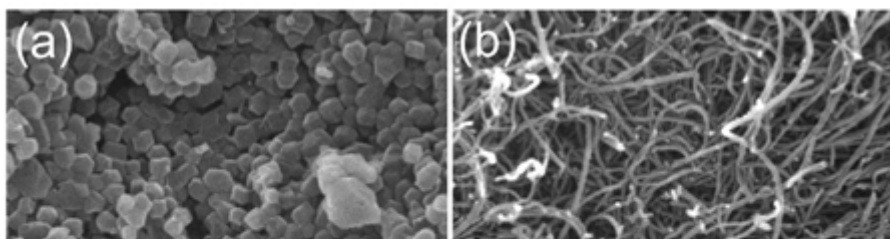
Figures

Figure 1

SEM images of ZIF-8 (a), MWCNTs (b), Fe-ZIF-8 (c) and FZM(d).
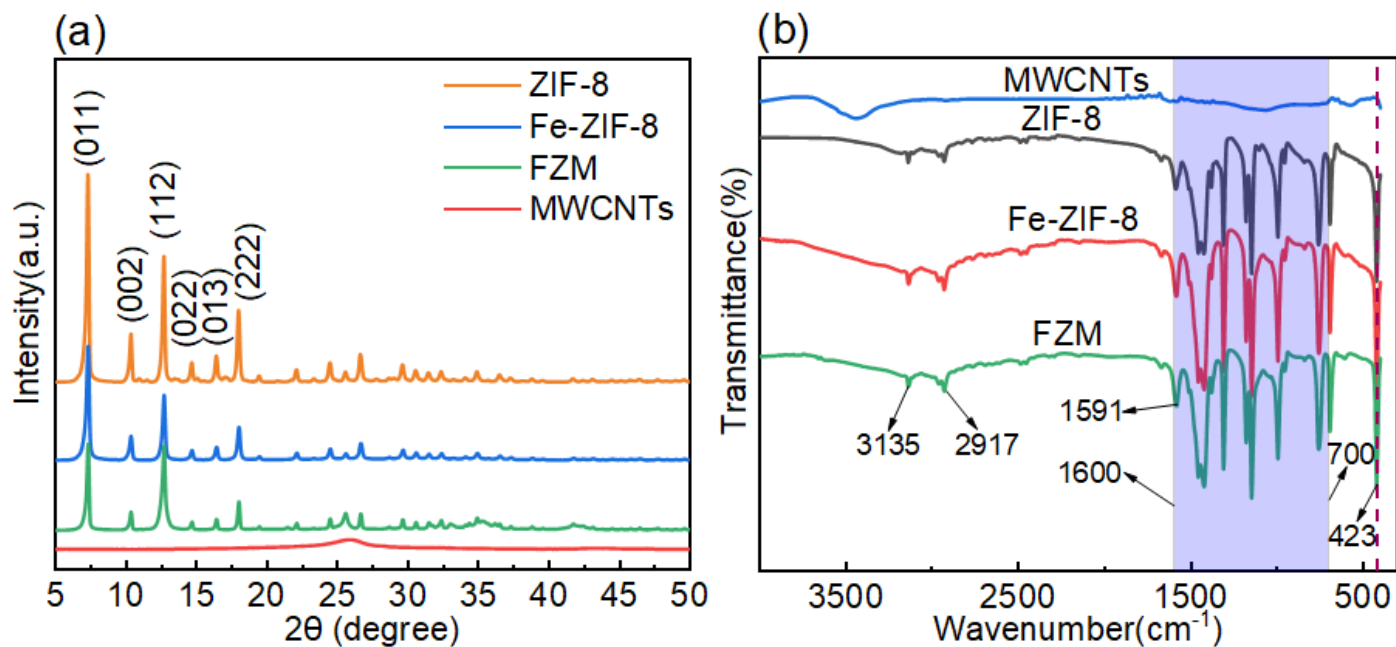
Figure 2

X-ray diffraction patterns of ZIF-8, MWCNTs, Fe-ZIF-8, and FZM(a); FTIR spectra of MWCNTs, ZIF-8, Fe-ZIF-8, and FZM(b).
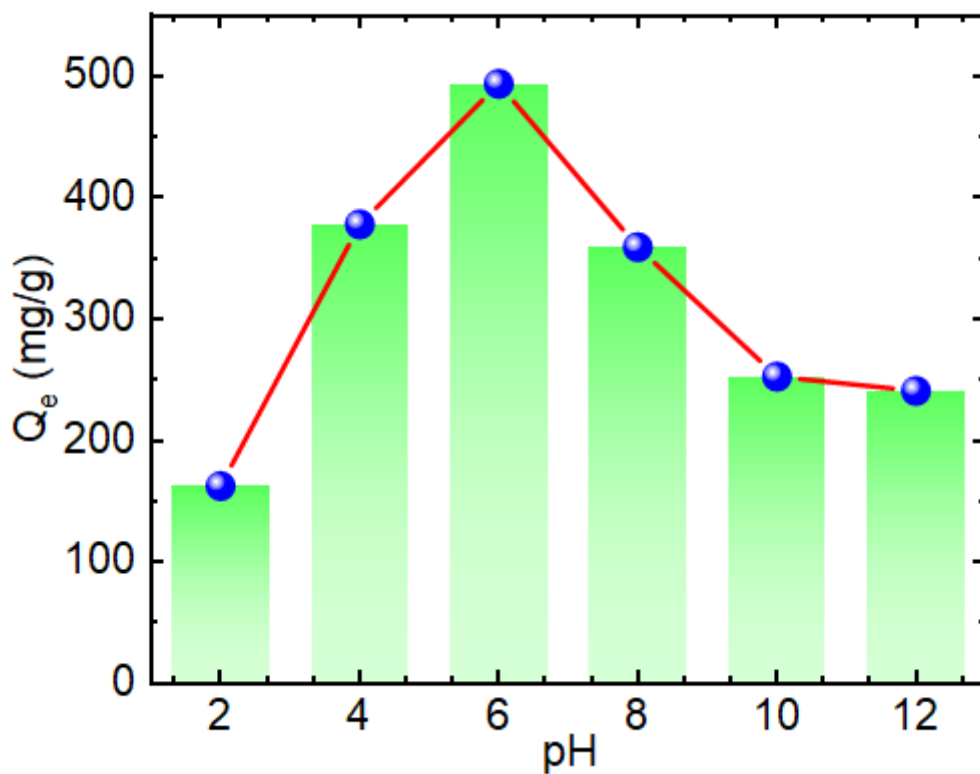

Figure 3

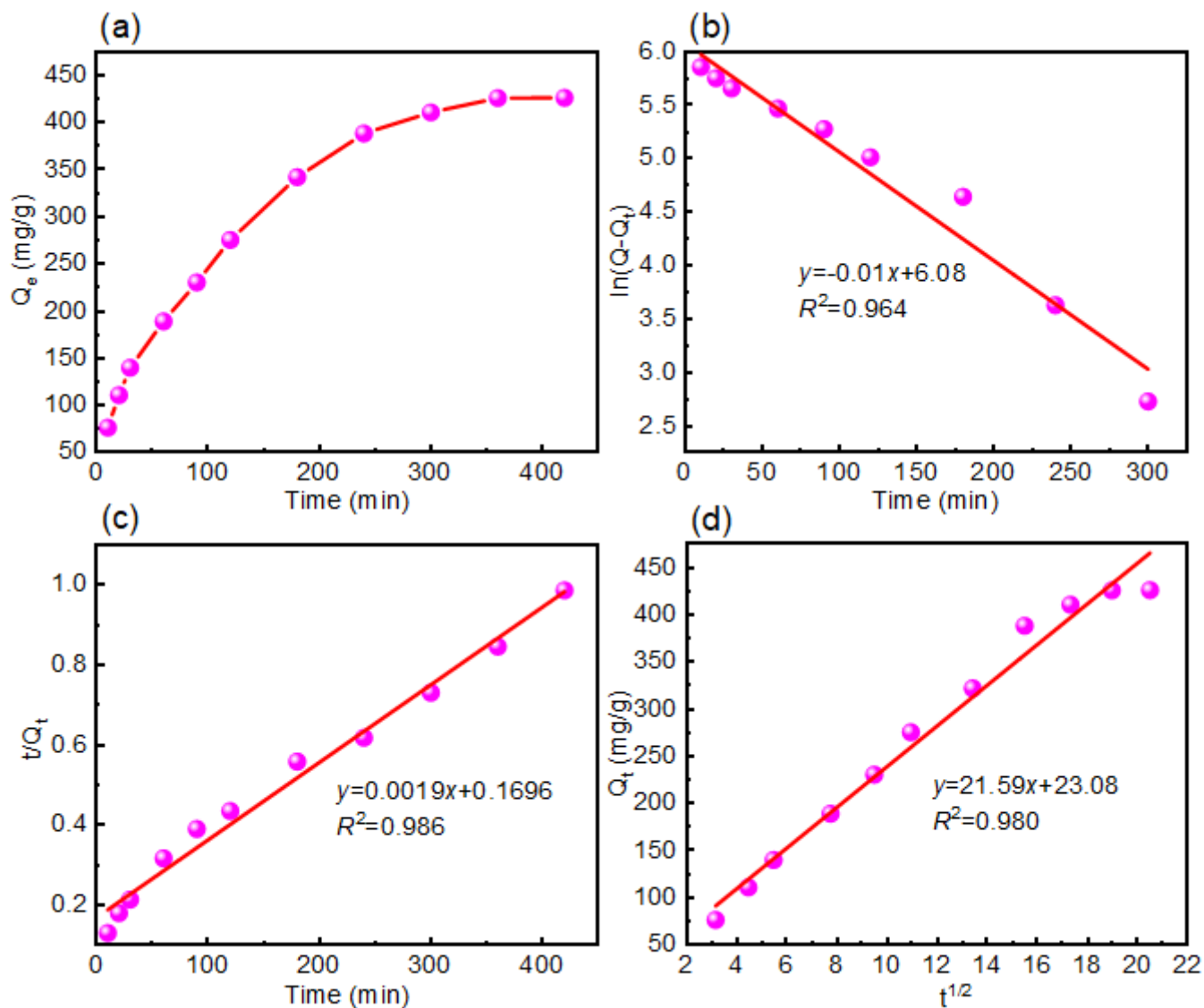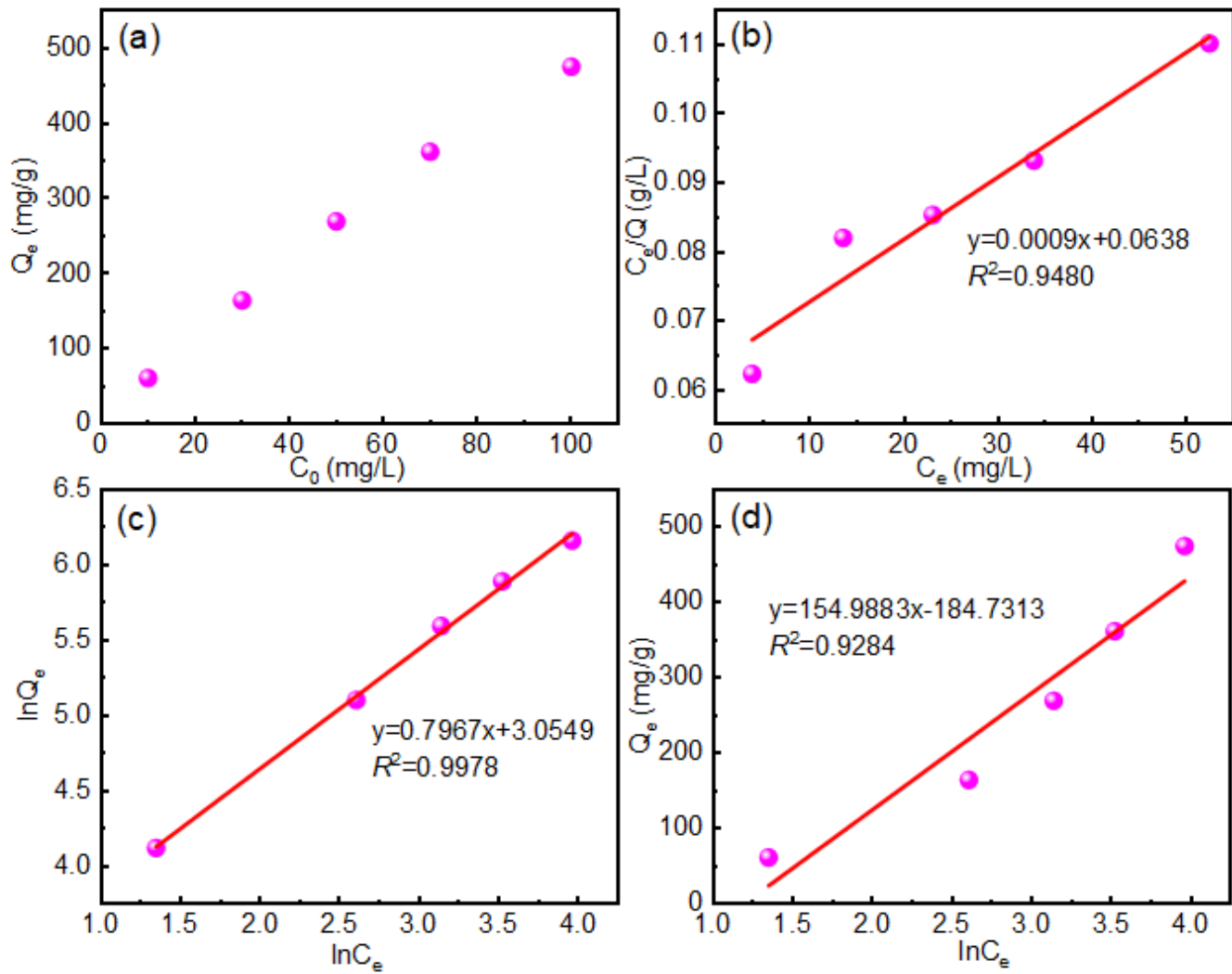Effect of initial solution pH on TC adsorption by FZM.

Figure 4

Effect of contact time on the adsorption of TC by FZM (a); the fitting results of the adsorption kinetic models of PFO (b), PSO (c), and ID (d).

Figure 5

Effect of concentration on the adsorption of TC by FZM (a); the data fitting results of Langmuir (b), Freundlich (c), and Temkin (d) adsorption isotherms
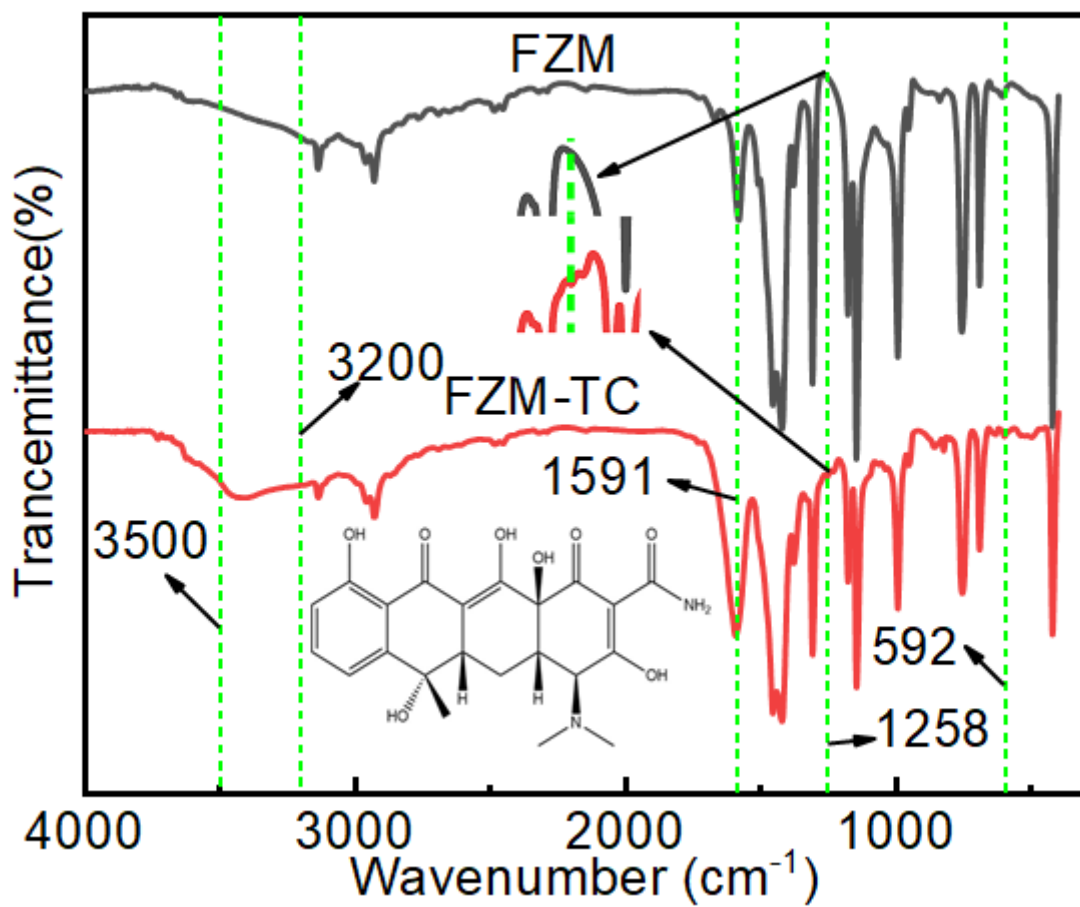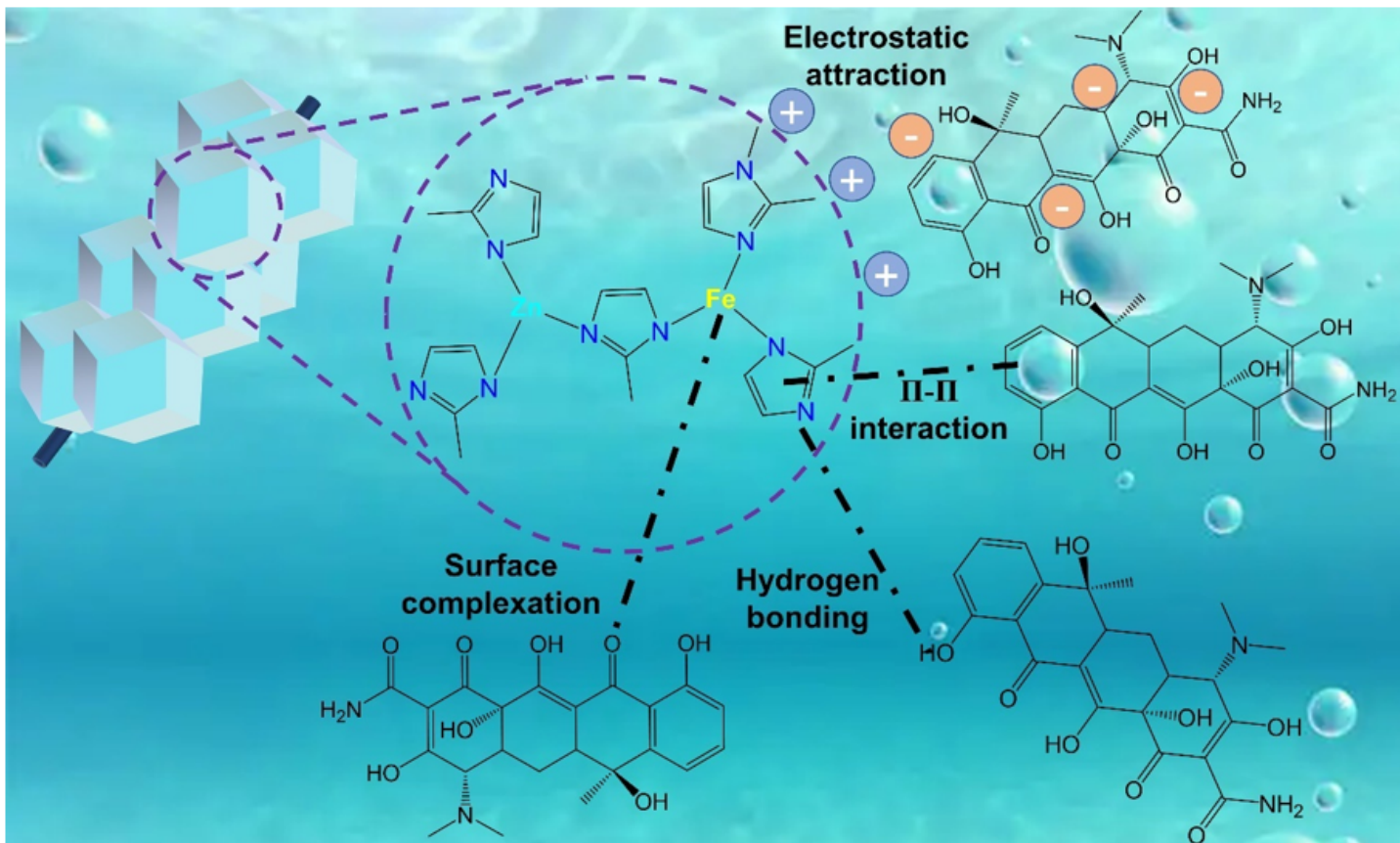
Figure 6

FTIR spectra of FZM before and after adsorption of TC

Figure 7

Possible adsorption mechanism diagram of TC on FZM

Figure 8

Contour plots and three-dimensional response plots of FZM adsorbed TC: pH - temperature (a, b); pH - dosage (c, d); temperature and dosage (e, f).

Figure 9

Effect of the number of cycles of FZM on the adsorption effect of TC

Supplementary Files

This is a list of supplementary files associated with this preprint. Click to download.

- SupplementaryInformation.docx